Journal of Materials Chemistry A

ROYAL SOCIETY OF CHEMISTRY

PAPER

View Article Online
View Journal | View Issue

Cite this: J. Mater. Chem. A, 2024, 12, 33984

Cold sintering of nickel manganese oxide for thermistor fabrication

Julian Fanghanel, *[ab] Satoshi Yokomizo,[c] Shuichi Funahashi[c] and Clive A. Randall*[ab]

Received 7th September 2024
Accepted 11th November 2024

DOI: 10.1039/d4ta06380e

rsc.li/materials-a

In this paper we successfully densified $NiMn_2O_4$ (NMO) ceramics using the cold sintering process (CSP) with various molten salt fluxes as a transient liquid phase, achieving relative densities exceeding 95%. The resulting samples exhibited comparable properties to conventionally sintered counterparts, demonstrating the feasibility of the CSP for NMO thermistor production. Electrical characterization revealed NMO samples sintered *via* CSP exhibited negative temperature coefficient (NTC) behavior with material constants (B) and temperature coefficients of resistivity (α) akin to conventionally sintered materials in the range of 3500–4300 K and 0.04–0.05 K^{-1}. Despite slightly higher resistances attributed to differences in grain size and impurities, the CSP-produced NMO samples remained within the typical range for NTC thermistors.

1. Introduction

The Cold Sintering Process (CSP) is the process of densifying ceramics, composites and metals at low temperatures[1,2] (<400 °C) through the use of directional compression of modest pressures ~100 MPa and a transient liquid phase.[3] Since the initial reporting of low temperature sintering[4] there are now over 150 different materials and compositions that have been successfully cold sintered under these conditions.[5,6] It is believed that CSP works with a sequential series of mechanisms including chemomechanical enhanced dissolution, transport and precipitation through a low temperature process called pressure solution creep.[7] This phenomenon was first introduced in the geological sciences in the late 19 century by Clifton Sorby,[8] and over the last 160 years, has attracted more sophisticated non-equilibrium thermodynamics approaches and been applied to and describes the process of formation densification of sedimentary rock within the Earth's crust.[9–11] The main principle of this phenomena is the idea that a directional pressure will increase the chemical potential in a transient liquid phase where the grains that are pressing against other grains are in the presence of this liquid (see Fig. 1). Through the increase in the local chemical potential with the dissolution of the chemical species from the particles, the areas of higher chemical potential will preferentially transport the solute species to the areas of low chemical potential along the grain boundary to areas such as triple points and pores in the material, where the pressure and chemical potential is lower. With the local heating, evaporation increases the concentration in the solution and then supersaturates and precipitates in these regions of lower chemical potential.[12–15] It is this dissolution, transport, and precipitation sequence that allows for removal of the curved surfaces at the particle contacts. This process transports matter to then close pores and triple points densifying the ceramic material and minimizing the excess surface energy.

The ability to densify ceramics and composites at low temperatures is very attractive as the world looks to find new ways to limit energy consumption and CO_2 emissions. Negative Temperature Coefficient (NTC) ceramic materials are a material that under conventional sintering conditions requires high sintering temperatures and long sintering times. In addition, the sintering profiles have complex exsolution reactions, and large changes in the defect chemistry and compensation

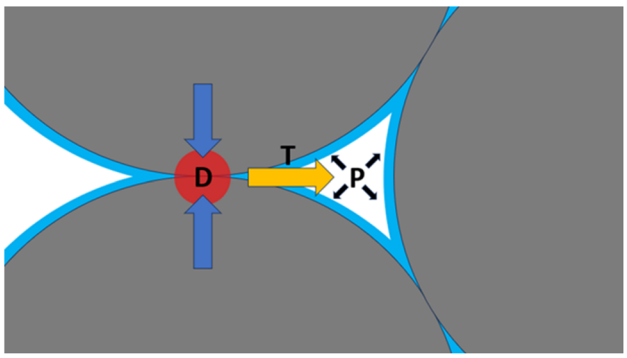

Fig. 1 Diagram of pressure solution creep where D is the area where dissolution occurs, T is the transport away from the high chemical potential, and P is the area of precipitation inside the triple points.

[a]Department of Materials Science and Engineering, The Pennsylvania State University, University Park, PA, 16802, USA. E-mail: juf624@psu.edu
[b]Materials Research Institute, The Pennsylvania State University, University Park, PA, 16802, USA
[c]Murata Manufacturing Co., Ltd., Nagaoka Division, R&D 26-10, Tenjin 2-Chome, Nagaokakyo-shi, Kyoto, Japan

mechanisms that are challenges in the property and quality control of manufacturing.

Thermistors are a type of resistor that changes its electrical resistance in response to changes in temperature. It is widely used in a variety of applications that need highly accurate temperature sensing. Thermistors are made of semiconducting oxide materials with a high temperature coefficient of resistance, meaning that their resistance changes significantly with temperature. There are two types of thermistors: negative temperature coefficient (NTC) and positive temperature coefficient (PTC) thermistors. NTC thermistors have a decreasing resistance with increasing temperature, while PTC thermistors have an increasing resistance with increasing temperature.

Spinel-structured AB_2O_4 manganese-based transition-metal oxide ceramics are the most commonly used materials for NTC thermistors, and are attractive for a wide range of applications due to their high temperature sensitivity, fast response time, circuit protection, ease of use, and affordability. There are many applications that need the accurate monitoring of temperatures including in manufacturing processes, engine operation, battery charging and monitoring, heating systems, medical health monitors and a wide variety of household instruments.

The key electrical properties of NTC ceramics for temperature measurement applications includes the materials constant (B), the room temperature coefficient resistance (ρ_{25}), and the temperature coefficient of resistivity (α).[16] The temperature dependence of the resistivity decrease depends on the experimental relationship given by:

$$\rho(T) = \rho_O \exp\left(\frac{B}{T}\right) \quad (1)$$

ρ_O is the pre-exponential and resistivity at infinite temperature.

B, the materials constant relates to the activation process, and T is absolute temperature.

The TCR then becomes:

$$\alpha_r = \frac{1}{R}\frac{dR}{dT} = -\frac{B}{T^2} \quad (2)$$

$NiMn_2O_4$ (NMO) is a complex oxide material with a spinel crystal structure that has cation sublattice with tetrahedral and octahedral sites (referred to as A site and B sites, respectively) along with oxygen sublattice forming an FCC oxygen sublattice. There are 8-formulae cells that make up the elementary cell, with a cube F-centered space group symmetry, $Fd3m$. In NMO the site occupancy, and decomposition reactions at high temperatures make the system very complex. Some of the reactions of importance under conventional sintering conditions include the following.

Above 900 °C, $NiMn_2O_4$ decomposes with the following reaction:

$$NiMn_2O_4 \leftrightarrow xNiO + x/6O_2 + (3 - x)/3Ni_{(3-3x/3)}Mn_{6/(3-x)}O_4 \quad (3)$$

Below, 750 °C, $NiMn_2O_4$ decomposes with the following reactions:[16–20]

$$NiMn_2O_4 + 1/4O_2 \leftrightarrow 1/2Mn_2O_3 + NiMnO_3 \quad (4)$$

The thermal process at high temperature and on cooling can lead to the tetrahedral site having different occupancies of Ni^{2+}, Mn^{2+}, and Mn^{4+}, and on the octahedral site can have Ni^{2+}, Mn^{3+} and Mn^{4+}.[9]

The resistivity of the NTC material is tied to the mixed valence of the manganese cations in the structure, as it is the electron polaron hopping along the chains of Mn^{3+} and Mn^{4+} ions that control the resistivity and activation energy.[18,21]

The decomposition and formation of other phases affects the electrical performance of the device. As NiO precipitates, the Ni^{2+} ions in the octahedral sites are removed from the structure, thus the amount of Mn^{3+} and Mn^{4+} ions must decrease to maintain charge balance. As a result, the electrical conductivity decreases.[16,20]

During conventional sintering of this material, it has been shown that sintering at temperatures below 975 °C cannot typically produce materials with densities larger than 95% no matter the length of time of sintering. Higher temperatures around 1000 °C and long sintering times close to 40 hours are needed to achieve consistently high densities greater than 95%.[17] This method also requires a secondary annealing temperature in the spinel stability region (~800 °C) to re-oxidize the decomposed spinel to form a single phase materials.[16,17] Per eqn (3), it is possible to have reoxidation in porous materials that allow oxygen to diffuse into the material.[17] Due to the inherent instability of this material at its sintering temperature, the high sintering temperatures, and long sintering times, it is important to research alternative methods of sintering this material at low temperatures such as with the CSP.

The CSP of nickel manganite, $NiMn_2O_4$ (NMO), has previously been attempted by Funahashi *et al.*[22] Where they used the aid of chelating nickel and manganese acetyl acetonate to sinter the samples. Here a ~88% relative density was obtained with a high resistivity (24 kΩ cm^{-1}) but a similar B constant as their conventionally sintered samples. The low carrier mobility in their samples was likely due to the low density, impurities and large numbers of grain boundaries relative to the larger grain sizes in the conventional sintered samples. This relatively low density is potentially problematic and hence the focus of research here will be to improve properties and density with the search of new transient phases in the CSP.

The choice of transient liquid phases that enable CSP requires it to drive dissolution, and the complexity needs to be sufficiently low to permit reversible precipitation, as outlined in the use of organic acids with ZnO.[23] Other transient phases that have been effective in the CSP process have been with hydroxide fluxes, which are abundantly used for the sintering of materials such as beta alumina,[24] NASICON ($Na_3Zr_2Si_2PO$),[25] potassium–sodium niobate,[26] and many others.

The general properties that an ideal flux for CSP should have the following characteristics: solubility for the solutes, a change in solubility with pressure, a low melting point, low viscosity for

increased diffusion, low corrosion of the dies and easily available.[27]

Molten salt fluxes are known to be very effective in the growth of various single crystals. In the case of spinel such as NMO Bi_2O_3–B_2O_3 has been used as a flux.[28] Other, spinel systems like $LiNi_{0.5}Mn_{1.5}O_{4-\delta}$ have used fluxes such as the LiCl–KCl system,[29] and $MgAl_2O_4$ and $CoAl_2O_4$ have been made using a flux of $Na_2B_4O_7$.[30] The spinels such as $MgFe_2O_4$, $MgAl_2O_4$ and $MgCr_2O_4$ have also been grown using NaBr or KBr.[31] Manganese oxides such as Li_2MnO_3 were made using LiOH, LiCl and LiCl–Li_2CO_3 fluxes. $LiMnO_2$ and Li_2MnO_3 were made using Li_2CO_3–K_2CO_3 eutectic flux tetragonal Mn_3O_4, which is a distorted spinel structure crystals have been made with NaCl flux. δ-MnO_2 and $K_xMn_8O_{16}$ ($x \leq 2$) were also produced in a flux of KNO_3.[32]

In this work, NMO powder has been densified using the CSP to obtain single cubic phase NMO dense ceramics. We will contrast the CSP with some selective fluxes with structural property relations.

2. Experimental method

2.1 Powder synthesis of $NiMn_2O_4$

A well crystallized, nanosized powder is synthesized *via* a sol–gel process, where 2.788 g of $NiCl_2$ (98%, Aldrich), and 7.933 g of $MnCl_2 \cdot 4H_2O$ (>98%, Sigma-Aldrich) were dissolved in 40 mL of water at 50 °C. After stirring for 15 minutes, 6 mL of sorbitol F solution (70 wt% in H_2O, Sigma-Aldrich) was slowly added. The resulting solution was heated and magnetically stirred for 3 hours, and then placed in an oven at 120 °C overnight to dry. The resulting gel was calcined at 800 °C for 3 hours at a heating rate of 10 °C min^{-1}. The resulting powder was then ground and immersed in a vial with ethanol and sonicated for 1 h. The ethanol is then evaporated by placing the vial in an oven at 80 °C overnight.

2.2 Sintering

A 0.05 g of a eutectic mixture of LiCl–KCl, LiBr–KBr or LiCl–LiI was weighed and mixed with 2 drops of DI water (roughly 10 wt%) with a mortar and pestle. 0.45 g of NMO was then added to the mortar and thoroughly mixed until homogeneous. The powder was then loaded into a stainless-steel die with a TiCN coating (pellet press die sets) with an inner radius of 13 mm which had lightly been lubricated with oleic acid. Disposable 0.1 mm nickel foils (Alfa Aesar, 99.95%) were placed in between the die punches and the powder to minimize contamination and corrosion of the punches. Uniaxial pressure was then applied using a bench press (Carver®) equipped with heated platens. The platens were preheated to a temperature of 340 °C before the die was introduced. The heating jacket was wrapped around the die, heating was set to 400 °C, and CSP started by applying 335 MPa uniaxial pressure. The dwell time for all experiments was 4 hours starting at the time the temperature reached 400 °C. Once the time elapsed the die was removed, cooled to room temperature, and the pellet was extracted. See Fig. 2.

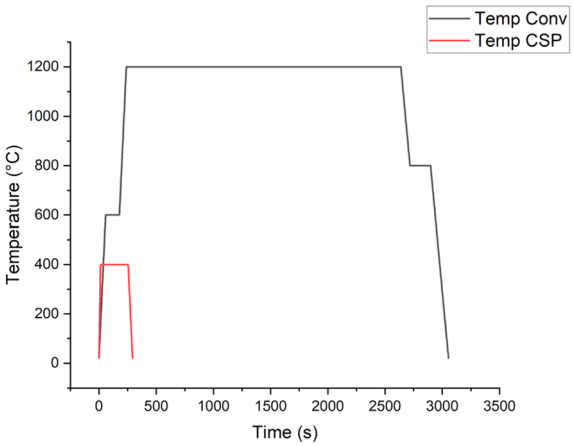

Fig. 2 Sintering profile for CSP (red) and conventional sintering (black).

As a control we conventionally sintered some ceramics at a temperature of 1200 °C for 40 hours and annealed at 800 °C for reoxidation for 3 hours.[17,19,20] Additionally, we also sintered NMO samples with 10 wt% flux of LiCl–KCl at 900 °C for 3 hours to establish if there is any benefit in using this flux as a sintering aid.

2.3 Characterizations

The density and relative density were measured geometrically using the average of 10 measurements of thickness and diameter and using Archimedes principle using 200 proof ethanol as the reference solvent, taking 5.12 g cm^{-3} as the theoretical density of NMO. X-ray diffraction (XRD) patterns were obtained using a PANanalytical Empyrean diffractometer in Bragg–Brentano configuration with operating parameters set to 45 kV and 40 mA. A 2θ range of 10–70 was scanned taking a step size of 0.026 with a Cu Kα radiation. Microstructure imaging was obtained by using a scanning electron microscope (SEM, Thermo Fisher FESEM Verios G4) on fracture surfaces coated with 5 nm of iridium using a sputter coater (Leica EM ACE600 sputter coater). The elemental distribution images of the microstructure were observed using electron dispersive spectroscopy (EDS) at 25 kV. Particle and grain size was determined by measuring over 400 grains in each case.

The current–voltage (I–V) analysis was performed on samples that were coated with conductive silver paint (Pelco®) using a Hewlett Packard 4140B pA meter/DC voltage source at a 1 V potential in the 20–50 °C range, with an incremental step of 5 °C. Experimental error was calculated using the least squared methods on the Arrhenius plot.

3. Results and discussion

3.1 Densification and microstructure

Through the use of the eutectic molten salt systems LiCl–KCl, LiBr–KBr, and LiCl–LiI as fluxes during the CSP, we produced ceramic samples of NMO that were successfully sintered into pellets of relative high density (>95%) on par with those of conventional sintered samples, see Table 1. These results

Table 1 Density, grain size, and electrical performance of sintering of $NiMn_2O_4$ by different sintering methods[a]

	Conventional sintering 1200 °C	Molten flux assisted sintering 900 °C	Cold sintering process
Relative density	99%	57.4%	96.8%[a], 96%[b], 97.3%[c]
Mean grain size (μm)	2.57	1.46	1.67[a], 1.84[b], 1.96[c]

[a] a = LiCl–KCl, b = LiBr–KBr, c = LiCl–LiI.

exceed those previously seen in the literature using low temperatures.[22]

Densification of NMO at 400 °C using a flux of the LiCl–KCl eutectic with a melting point of 347 °C has demonstrated good densification at low temperatures. The densities we were able to achieve were of 96.8% relative density, taking 5.21 g cm^{-3} as the theoretical density. It is clear from the SEM image in Fig. 3a that the densification of the samples leads to a substantial increase in particle size, and the grain size distribution, Fig. 3, is now of 4 different types of particles, with median sizes of 0.67, 4.62, 7.28, and 11.53 μm. It is evident from the images and the distribution that the particle size/grain size distribution shows that there is very little coarsening beyond a factor of 2–3× from the primary particle size. We believe the overall trend is consistent with Ostwald ripening.

The fact that there remains a large population of grains in the smaller range circa the original 0.42 μm, alludes to the precipitation mechanism of our oxide during CSP. Additionally, we can observe that the morphology of the prismatic crystals is conserved.

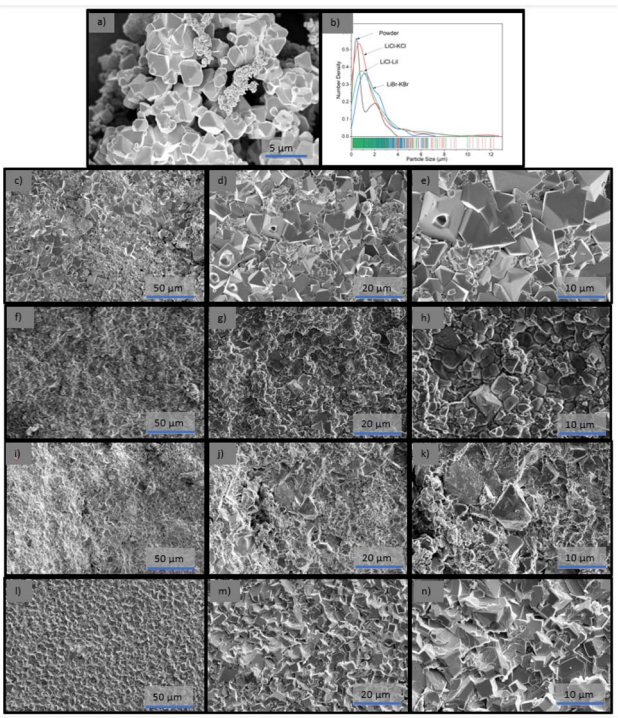

Fig. 3 SEM images of (a) reference powder image with (b) the particle/grain size distribution for each sample, (c–e) CSP with LiCl–KCl, (f–h) LiBr–KBr, (i–k) LiCl–LiI, (l–n) conventionally sintered.

The use of the fluxes LiBr–KBr and LiCl–LiI with a sintering temperature of 400 °C and a melting point of 321 °C and 367 °C respectively for both systems, have produced dense ceramic samples. The properties can be seen in Table 1. The relative density achieved with the LiBr–KBr flux was 96.0%. SEM images show that the densification of the samples occurred, and the prismatic crystals shape was not preserved. The particle size distribution shows that there are 4 sets of particles with median values at 1.15 μm, 2.18 μm, 4.44 μm, and 6.16 μm. This distribution shows us that there is an overall increase in particle size. The smaller particles are absent in this sample and the distribution of large particles shifts our curve to the right.

For the LiCl–LiI system the relative density achieved was 97.3%. We can see in the SEM images in Fig. 3 that even though there are large crystals that retain some partial prismatic crystal morphology, most of the other grains do not. It is unclear if the large areas of rough morphology throughout the pellet are constituted by very large grains with rough surfaces or if they are composed of very small individual grains. The particle size distribution shows 3 distinct particle sizes with the median at 0.90, 6.43 and 10.08 μm. This particle size/grain size distribution once again shows that there is very little coarsening beyond a factor of 2–3× from the primary particle size. We believe the overall trend is consistent with Ostwald ripening.

3.2 Electrical characterization

Fig. 4 shows plots of log(r) as a function of reciprocal of absolute temperature (1000/T) for our samples. We observed that the relationship between ln(r) and 1000/T is linear in which the resistance of our material decreases with increasing temperature. This is consistent with NTC characteristics. B and α constants in Table 2 are calculated from the resistance R_1 at T_1 = 20 °C and R_2 at T_2 = 50 °C.

$$\ln(r) = \ln(r_0) + \frac{B}{T} \tag{5}$$

$$B = \frac{\ln\left(\frac{r_1}{r_2}\right)}{\frac{1}{T_1} - \frac{1}{T_2}} \tag{6}$$

where B is the materials constant, r is the resistance, r_0 is the resistance at infinite temperature, and T is temperature.

In Table 2 we can see that the properties of our samples made using the CSP have B and α on par with that of conventionally sintered samples. It is in our resistance that our samples using CSP differ, with those made by CSP having

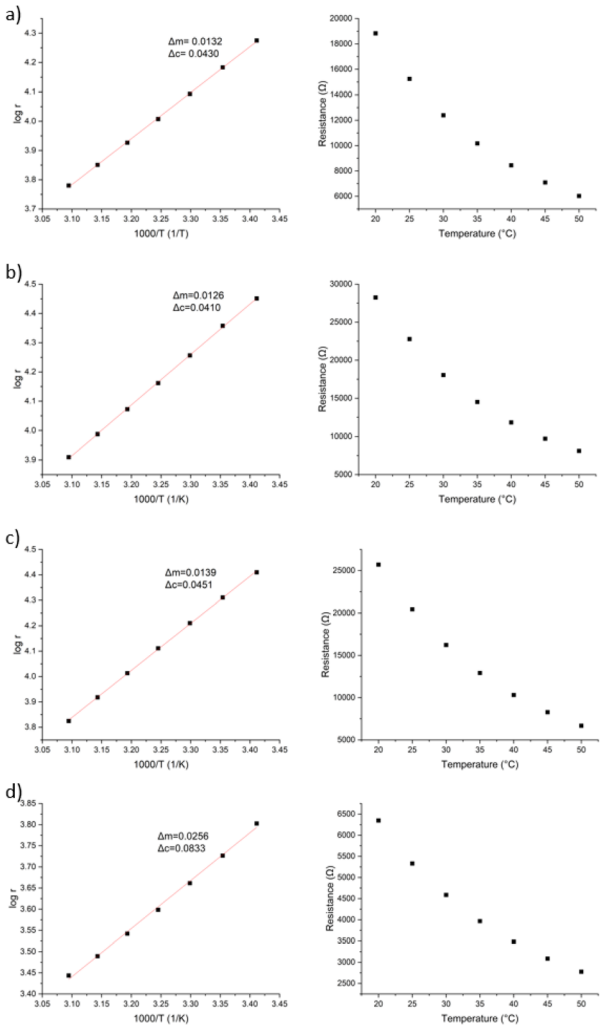

Fig. 4 Arrhenius plot and resistance *vs.* temperature data of (a) LiCl–KCl flux, (b) LiBr–KBr flux, (c) LiCl–LiI flux, (d) conventionally sintered.

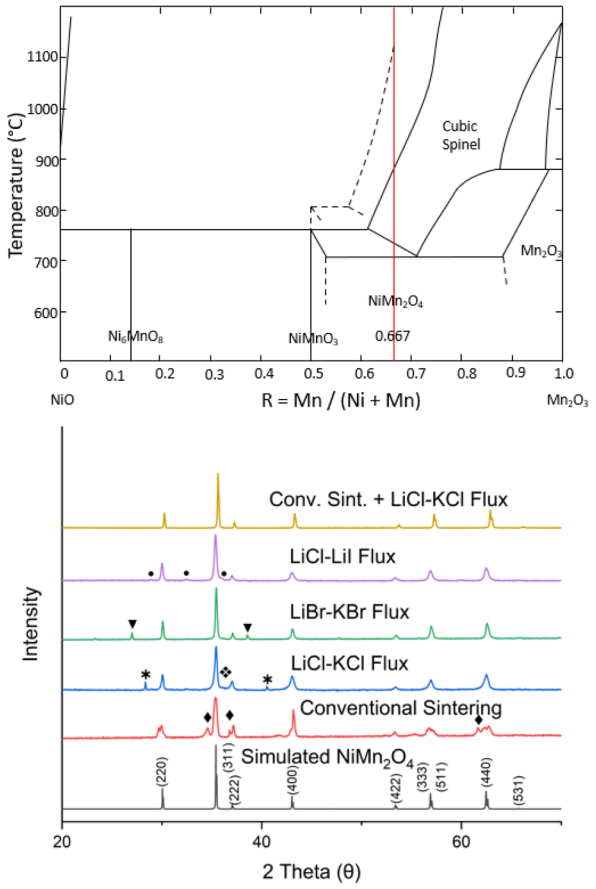

Fig. 5 Phase diagram of $NiO–Mn_2O_3$ system[34] and XRD pattern of our samples. With identified impurities labelled as * = KCl, ❖ = Mn_2O_3, ▼ = KBr, ◆ = NiO, • = $LiMn_2O_4$.

a much higher resistance than those made by conventional sintering. This is likely due to differences in grain size and impurities from the flux causing carrier mobility to be low in CSP samples. That being said, it is considered to be in the range of typical NTC thermistors to exhibit resistances between 1 kΩ to 1000 kΩ.[19]

3.3 Phase purity

One of the main issues with the conventional sintering of NMO is that at its sintering temperature (>900 °C), there is decomposition of the material and other phases form. These can then be minimized by the reoxidation of the material at ~800 °C to try to make single phase cubic spinel NMO, as can be seen in the phase diagram on Fig. 5. We can see in our XRD of our final pellets that the degree of decomposition of NMO in general remains minimal with the addition of some small peaks of our flux. This is not what we see with our conventionally sintered samples, and our samples using LiCl–KCl where we see more decomposition. We believe that this decomposition and additional phases in the material made it particularly hard for us to obtain good electrical properties from our conventionally sintered samples, even those that exhibited 99% density. We see in this figure that the conventionally sintered samples degrade into the manganese rich spinel and nickel oxide, as well as peak splitting on the (220) family, likely related to the decomposition of the material. For our LiCl–KCl flux, we see evidence of the

Table 2 Electrical properties of CSP and conventionally sintered samples

Flux/method	Conventional sintering	$Ni_{0.6}Co_{0.3}Mn_{2.1}O_4$	LiCl–KCl	LiBr–KBr	LiCl–LiI
B (K)	2610	3600 (ref. 33)	3597	3937	4258
r_{25} (kΩ)	5.33	100 (ref. 33)	15.2	22.8	20.4
α_{25} (K^{-1})	−0.03	−0.04 (ref. 33)	−0.04	−0.04	−0.05

evolution of Mn_2O_3 spinel which is particularly interesting as we never reach the decomposition temperature using the CSP. As such, this is something worth studying further in future work as it can elucidate the mechanisms through which CSP is taking place. Lastly for the LiCl–LiI flux, we find traces of a secondary phase, $LiMn_2O_4$. A secondary phase is to be expected with this flux as Lithium iodide is unstable and the flux's I^- ions oxidize to form I_2 which then sublimes, leaving behind lithium that incorporates and forms a secondary phase. The impressive thing about this flux is that it provided the highest density compared to the other fluxes, while being unstable.

3.4 Other thermistor chemistries and spinels

Though not all thermistors are made using the chemical composition used in this paper, we hypothesise that this work can surely be used as a foundation to look at other Mn : Ni ratios and other spinel chemistries in the future. Though the same flux chemistries are not guaranteed to work, our hypothesis is that these fluxes and or similar flux concepts could work well across the spinels family, as several spinels and manganese oxides share similar fluxes used for their crystal growth.

4. Conclusions

We have managed to densify NMO using a series of molten salts (fluxes) as the transient liquid phase during CSP that resulted in pellets of densities over 95%. The properties achieved with these samples show they are on par with those of conventionally sintered samples and have properties consistent with those needed for the application of NMO thermistors. The use of molten salts as fluxes in the CSP has many advantages, as we decrease the energy consumption, the processing time, as well as reduce decomposition of our material. We believe that continued study is needed to understand the role of fluxes as a transient liquid phase and what insights we can pull from the crystal growth field.

Data availability

The authors confirm that the data supporting the findings of this study are available within the article.

Author contributions

Conceptualization, J. F., C. A. R.; methodology, J. F., C. A. R.; investigation, J. F., S. Y., S. F.; formal analysis J. F.; supervision, C. A. R.; writing – original draft, J. F.; writing – review and editing, J. F., S. Y., S. F., C. A. R.; funding acquisition, C. A. R.; project administration, C. A. R.

Conflicts of interest

The authors declare no competing financial interest.

Acknowledgements

The authors would like to acknowledge the financial support for this work provided by The Murata Manufacturing Company. The authors would also like to thank the Materials Characterization Laboratory of the Materials Research Institute at the Pennsylvania State University for aiding in the collection of the data.

References

1 S. Shetty, P. Numkiatsakul, K. Wickline, R. Incarnato, H. Wang, H. Kunkel, C. A. Randall and S. Trolier-Mckinstry, *IEEE Trans. Ultrason. Ferroelectr. Freq. Control*, 2022, **69**, 1413–1427.
2 L. Paradis, D. Waryoba, K. Robertson, A. Ndayishimiye, Z. Fan, R. Rajagopalan and C. A. Randall, *Adv. Eng. Mater.*, 2022, **24**, 2200714.
3 H. Guo, J. Guo, A. Baker and C. A. Randall, *ACS Appl. Mater. Interfaces*, 2016, **8**, 20909–20915.
4 H. Kähäri, M. Teirikangas, J. Juuti and H. Jantunen, *J. Am. Ceram. Soc.*, 2014, **97**, 3378–3379.
5 S. Grasso, M. Biesuz, L. Zoli, G. Taveri, A. I. Duff, D. Ke, A. Jiang and M. J. Reece, *Adv. Appl. Ceram.*, 2020, **119**, 115–143.
6 C. Vakifahmetoglu and L. Karacasulu, *Curr. Opin. Solid State Mater. Sci.*, 2020, **24**(1), 100807.
7 A. Ndayishimiye, S. H. Bang, C. J. Spiers and C. A. Randall, *J. Eur. Ceram. Soc.*, 2023, **43**, 1–13.
8 H. Clifton Sorby, *J. Franklin Inst.*, 1864, **77**, 97–106.
9 E. H. Rutter and D. Elliott, *Philos. Trans. R. Soc. London*, 1976, **283**(1312), 203–219.
10 S. Karato, *Deformation of Earth Materials*, Cambridge University Press, 2008.
11 S. Nakashima, *Tectonophysics*, 1995, **245**(3–4), 185–203.
12 H. Guo, A. Baker, J. Guo and C. A. Randall, *ACS Nano*, 2016, **10**, 10606–10614.
13 J.-P. Maria, X. Kang, R. D. Floyd, E. C. Dickey, H. Guo, J. Guo, A. Baker, S. Funihashi and C. A. Randall, *J. Mater. Res.*, 2017, **32**, 3205–3218.
14 S. Funahashi, J. Guo, H. Guo, K. Wang, A. L. Baker, K. Shiratsuyu and C. A. Randall, *J. Am. Ceram. Soc.*, 2017, **100**, 546–553.
15 A. Galotta and V. M. Sglavo, *J. Eur. Ceram. Soc.*, 2021, **41**, 1–17.
16 C. Ma and H. Gao, *J. Mater. Sci.: Mater. Electron.*, 2017, **28**, 6699–6703.
17 J. Jung, J. Töpfer, J. Mürbe and A. Feltz, *J. Eur. Ceram. Soc.*, 1990, **6**, 351–359.
18 G. D. C. Csete de Györgyfalva and I. M. Reaney, *J. Eur. Ceram. Soc.*, 2001, **21**, 2145–2148.
19 T. Reimann and J. Töpfer, *J. Mater. Sci.: Mater. Electron.*, 2021, **32**, 10761–10768.
20 A. Feltz, J. Töpfer and F. Schirrmeister, *J. Eur. Ceram. Soc.*, 1992, **9**, 187–191.
21 M. Hosseini, *Ceram. Int.*, 2000, **26**, 245–249.

22 S. Funahashi, E. Kobayashi, M. Kimura, K. Shiratsuyu and C. A. Randall, *J. Ceram. Soc. Jpn.*, 2019, **127**, 899–904.
23 A. Jabr, J. Fanghanel, Z. Fan, R. Bermejo and C. Randall, *J. Eur. Ceram. Soc.*, 2023, **43**, 1531–1541.
24 Z. Grady, A. Ndayishimiye and C. Randall, *J. Mater. Chem. A*, 2021, **9**, 22002–22014.
25 Z. M. Grady, K. Tsuji, A. Ndayishimiye, J. Hwan-Seo and C. A. Randall, *ACS Appl. Energy Mater.*, 2020, **3**, 4356–4366.
26 K. Tsuji, Z. Fan, S. H. Bang, S. Dursun, S. Trolier-McKinstry and C. A. Randall, *J. Eur. Ceram. Soc.*, 2022, **42**, 105–111.
27 M. Tachibana, *Beginner's Guide to Flux Crystal Growth*, Springer Japan, Tokyo, 2017.
28 H. Makram, *J. Cryst. Growth*, 1967, **1**, 325–326.
29 S. L. Spence, Z. Xu, S. Sainio, D. Nordlund and F. Lin, *Inorg. Chem.*, 2020, **59**, 10591–10603.
30 V. D'Ippolito, G. B. Andreozzi, F. Bosi and U. Halenius, *Am. Mineral.*, 2012, **97**, 1828–1833.
31 V. V. Klepov, C. A. Juillerat, K. A. Pace, G. Morrison and H. C. zur Loye, *Front. Chem.*, 2020, **8**, 1–18.
32 X. Yang, W. Tang, Q. Feng and K. Ooi, *Cryst. Growth Des.*, 2003, **3**, 409–415.
33 A. J. Moulson and J. M. Herbert, *Electroceramics: Materials, Properties, Applications*, Wiley, 2003.
34 D. G. Wickham, *J. Inorg. Nucl. Chem.*, 1964, **26**, 1369–1377.